

LETTER TO THE EDITOR

Chemical segregation in the young protostars Barnard 1b-N and S

Evidence of pseudo-disk rotation in Barnard 1b-S^{★,★★}

A. Fuente¹, M. Gerin², J. Pety^{2,3}, B. Commerçon⁴, M. Agúndez⁵, J. Cernicharo⁵, N. Marcelino⁵, E. Roueff², D. C. Lis², and H. A. Wootten⁶

¹ Observatorio Astronómico Nacional (OAN, IGN), Apdo 112, 28803 Alcalá de Henares, Spain
e-mail: a.fuente@oan.es

² LERMA, Observatoire de Paris, PSL Research University, CNRS, Sorbonne Universités, UPMC Univ. Paris 06, École Normale Supérieure, 75005 Paris, France

³ Institut de Radioastronomie Millimétrique (IRAM), 300 rue de la Piscine, 38406 Saint Martin d'Hères, France

⁴ Centre de Recherche Astronomique de Lyon (CRAL), École Normale Supérieure de Lyon, CNRS-UMR 5574, 69364 Lyon Cedex 07, France

⁵ Instituto de Ciencia de Materiales de Madrid (ICMM-CSIC). 28049 Cantoblanco, Madrid, Spain

⁶ National Radio Astronomy Observatory, 520 Edgemont Road, Charlottesville, VA 22903, USA

Received 10 April 2017 / Accepted 18 August 2017

ABSTRACT

The extremely young Class 0 object B1b-S and the first hydrostatic core (FSHC) candidate, B1b-N, provide a unique opportunity to study the chemical changes produced in the elusive transition from the prestellar core to the protostellar phase. We present $40'' \times 70''$ images of Barnard 1b in the ^{13}CO $1 \rightarrow 0$, C^{18}O $1 \rightarrow 0$, NH_2D $1_{1,1}a \rightarrow 1_{0,1}s$, and SO $3_2 \rightarrow 2_1$ lines obtained with the NOEMA interferometer. The observed chemical segregation allows us to unveil the physical structure of this young protostellar system down to scales of ~ 500 au. The two protostellar objects are embedded in an elongated condensation, with a velocity gradient of ~ 0.2 – $0.4 \text{ m s}^{-1} \text{ au}^{-1}$ in the east-west direction, reminiscent of an axial collapse. The NH_2D data reveal cold and dense pseudo-disks ($R \sim 500$ – 1000 au) around each protostar. Moreover, we observe evidence of pseudo-disk rotation around B1b-S. We do not see any signature of the bipolar outflows associated with B1b-N and B1b-S, which were previously detected in H_2CO and CH_3OH , in any of the imaged species. The non-detection of SO constrains the $\text{SO}/\text{CH}_3\text{OH}$ abundance ratio in the high-velocity gas.

Key words. astrochemistry – ISM: clouds – ISM: individual objects: Barnard 1b – stars: formation – stars: low-mass – ISM: kinematics and dynamics

1. Introduction

Barnard 1b (B1b) is a well-known dark cloud located in the Perseus molecular cloud complex ($D = 230$ pc). Interferometric observations revealed two young stellar objects (YSOs), B1b-N and B1b-S, deeply embedded in a thick envelope (Huang & Hirano 2013) that is characterized by its large column density, $N(\text{H}_2) \sim 7.6 \times 10^{22} \text{ cm}^{-2}$ (Daniel et al. 2013), and low kinetic temperature, $T_k = 12 \text{ K}$ (Lis et al. 2010). Based on *Herschel* fluxes and subsequent spectral energy distribution modeling, Pezzuto et al. (2012) concluded that B1b-N and B1b-S were younger than Class 0 sources and proposed them to be first hydrostatic core (FHSC) candidates. Using NOEMA, Gerin et al. (2015) detected and imaged the protostellar outflows, confirming the young ages of B1b-N and B1b-S (~ 1000 yr and ~ 3000 yr) and the high-density environment (\sim a few 10^5 cm^{-3} for the outflowing gas). ALMA observations of B1b-N and B1b-S, at an unprecedented angular resolution, allowed detecting compact condensations of $0.2''$ and $0.35''$ radius (46 and 80 au) in B1b-N and B1b-S, respectively, in addition to a more

extended envelope (Gerin et al. 2017). The sizes and orientations of the compact structures are consistent with those of the disks formed in numerical simulations of collapsing cores (Gerin et al. 2017) in the very early phases (before Class 0) of the star formation process. The young protostars B1b-S and B1b-N are therefore promising objects to investigate the beginnings of the low-mass star formation process.

2. NOEMA observations

NOEMA observations were carried out during August and October, 2015 using seven antennas in its CD configurations. The 3 mm receivers were centered on ~ 110 GHz, covering the 109–111 GHz band. The wideband correlator WIDEX provided spectroscopic data of the whole band with a spectral resolution of ~ 2 MHz. Several 40 MHz units, providing a spectral resolution of 40 kHz, were centered on the frequencies of the intense lines ^{13}CO $1 \rightarrow 0$, C^{18}O $1 \rightarrow 0$, SO $3_2 \rightarrow 2_1$, NH_2D $1_{1,1}a \rightarrow 1_{0,1}s$, and HNCO $5_{0,5} \rightarrow 5_{0,4}$. After 16 h on-source, we obtained an rms of $\sim 0.20 \text{ K}$ at 40 kHz spectral resolution ($\sim 0.1 \text{ km s}^{-1}$) with an angular resolution of $\sim 5.0'' \times 3.4''$ (1155 au \times 785 au). The HNCO line has been barely detected, and its analysis is not included in this Letter.

In order to obtain a high-fidelity image of the entire cloud, we have combined NOEMA observations with short-spacing data. We used the IRAM 30 m telescope to map an area twice as large as the requested NOEMA map, that is, 9 arcmin square,

* Based on observations carried out with the IRAM Northern Extended Millimeter Array (NOEMA). IRAM is supported by INSU/CNRS (France), MPG (Germany), and IGN (Spain).

** The reduced datacube is only available at the CDS via anonymous ftp to [cdsarc.u-strasbg.fr \(130.79.128.5\)](http://cdsarc.u-strasbg.fr/130.79.128.5) or via <http://cdsarc.u-strasbg.fr/viz-bin/qcat?J/A+A/606/L3>

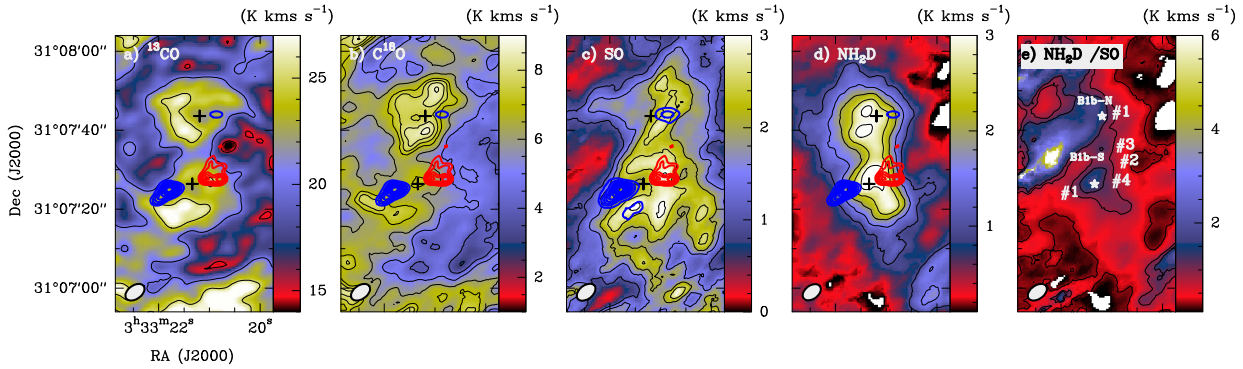


Fig. 1. Panel *a*: integrated intensity image (NOEMA+30 m) of the ^{13}CO $1 \rightarrow 0$ line. Contour levels are 15 ($\approx 150 \times \sigma$), 20 , and 25 K km s^{-1} . Crosses indicate the positions of B1b-N and S. The blue and red contours correspond to the blue and red lobes of the B1b-N and S bipolar outflows as traced by the H_2CO emission published by Gerin et al. (2015). The beam is plotted in the left bottom corner. Panel *b*: the same as *a*) for the C^{18}O $1 \rightarrow 0$ line. Contour levels are 4 ($\approx 40 \times \sigma$), 5 , 6 , 7 , 7.5 , 8 , and 8.5 km s^{-1} . Panel *c*: the same as *a*) for the SO $3_2 \rightarrow 2_1$ line. Contour levels are 1 ($\approx 10 \times \sigma$) to 8 in steps of 0.5 K km s^{-1} . Panel *d*: the same as *a*) for the integrated intensity of all the hyperfine components of the NH_2D $1_{1,1}a \rightarrow 1_{0,1}s$ line. Contour levels are 1 ($\approx 10 \times \sigma$) to 8 in steps of 0.5 K km s^{-1} . Panel *e*: $I(\text{NH}_2\text{D})/I(\text{SO})$ integrated intensity ratio (ratio between the images in panels *d* and *c*). The spectra toward the positions labeled in this panel are shown in Fig. A.1.

to fully recover the extended structure. Short-spacing data were merged with NOEMA observations using the GILDAS¹/CLASS software. Final images were created with a velocity resolution of 0.2 km s^{-1} for SO and the CO isotopologues, and of 0.14 km s^{-1} for the NH_2D lines. In this Letter we use the final 30 m+NOEMA cubes (see the observational parameters in Table A.1).

3. Large-scale morphology

The emission of all molecules traces the elongated ridge in which the two protostars and their associated outflows are embedded (see the integrated-intensity images in Fig. 1). Interestingly, the ^{13}CO $1 \rightarrow 0$, C^{18}O $1 \rightarrow 0$, and SO $3_2 \rightarrow 2_1$ maps do not present emission peaks toward the protostar positions, and only the NH_2D image shows local peaks toward B1b-N and B1b-S.

The ^{13}CO $1 \rightarrow 0$ brightness temperature varies between 5 and 11 K along the ridge (see Figs. 1 and A.1). The emission of this transition is expected to be optically thick in this high-extinction filament (Fuente et al. 2016), and its brightness temperature is a measure of the gas kinetic temperature. Assuming that the ^{13}CO emission is thermalized, which is reasonable for densities $n(\text{H}_2) > 10^4 \text{ cm}^{-3}$, the observed peak brightness temperatures imply gas kinetic temperatures of $T_k = 8\text{--}14 \text{ K}$. These values are in agreement with the averaged temperature of 12 K obtained from the ammonia lines by Lis et al. (2010). Toward B1b-N, the ^{13}CO and C^{18}O $1 \rightarrow 0$ lines present the same intensity, $T_b \sim 4 \text{ K}$ (Fig. A.1), consistent with optically thick gas at $T_k = 8 \text{ K}$. Toward B1b-S, the line profiles of the ^{13}CO and C^{18}O lines present self-absorption features that preclude an accurate estimate of the gas temperature. We can only derive a lower limit of $T_k > 14 \text{ K}$. This limit shows that the outflow has already heated the neighborhood of this protostar, as also demonstrated by the high temperatures (30–70 K) derived from the CH_3OH lines by Gerin et al. (2015).

The SO emission, and to a lesser extent C^{18}O , seem to surround the NH_2D peaks. In Fig. A.2 we show the channel velocity maps of the SO and NH_2D lines. The region of enhanced SO emission clearly surrounds the cold gas traced by NH_2D toward B1b-S. Toward B1b-N, the morphology of the emission is not that clear because the protostellar core is deeply embedded in the cold filament. It is noticeable that the line width of the

SO line is $\sim 1 \text{ km s}^{-1}$ throughout the region (see Fig. A.1 and Table A.2). The SO emission therefore does not arise from the high-velocity gas associated with the bipolar outflows detected by Gerin et al. (2015), but from the dense ridge, as suggested by Fuente et al. (2016).

The morphology of the NH_2D emission is most similar to that of the 1.2 mm continuum emission map reported by Daniel et al. (2013). This is confirmed by the $I(\text{NH}_2\text{D})/I(\text{SO})$ integrated-intensity map shown in Fig. 1e, which presents local maxima toward B1b-S and B1b-N. This deuterated compound is, thus far, our best candidate to probe the neighborhood of the protostars. In order to explore the gas kinematics in this complex star-forming region, in Fig. 2a we show the first-order moment map of the main hyperfine components of the NH_2D $1_{1,1}a \rightarrow 1_{0,1}s$ line. The entire molecular filament presents a velocity gradient in the direction perpendicular to the filament with velocities increasing from ~ 6.5 to 7.0 km s^{-1} from west to east ($\approx 0.2\text{--}0.4 \text{ m s}^{-1} \text{ au}^{-1}$) (see also Fig. A.2). This gradient suggests that the whole filament is contracting in the axial direction and that its fragmentation has driven to the formation of B1b-N and B1b-S. This overall east-west velocity gradient twists in the vicinity of B1b-S because this young protostellar object is formed there. The gas kinematics in the surroundings of B1b-S is discussed in detail in Sect. 4.

4. B1b-N and S bipolar outflows

In Fig. A.1 we compare our interferometric spectra with those of the H_2CO and CH_3OH lines published by Gerin et al. (2015) toward selected positions in the bipolar outflow lobes. Only the H_2CO and CH_3OH spectra show high-velocity wings (0.5 to 5.5 km s^{-1} and 7.5 to 12.5 km s^{-1} for the B1b-N outflow; -4.0 to 5.5 km s^{-1} and 7.5 to 15 km s^{-1} in the B1b-S outflow). The observed C^{18}O , SO, and NH_2D lines are very narrow with $\Delta v < 1 \text{ km s}^{-1}$ (see Table A.2). The line width of the ^{13}CO $1 \rightarrow 0$ line is larger, $\Delta v \sim 2 \text{ km s}^{-1}$, with emission in the velocity ranges of $4\text{--}5.5 \text{ km s}^{-1}$ and $7.5\text{--}8 \text{ km s}^{-1}$. However, the channel velocity maps do not show any correlation between the morphology of this moderate velocity gas and the lobes of the outflows. More likely, this emission comes from the more turbulent envelope (Daniel et al. 2013).

We did not detect high-velocity emission in the SO and ^{13}CO lines with an rms $\sim 0.06 \text{ K}$ ($\Delta v = 1 \text{ km s}^{-1}$). Assuming optically thin emission and the physical conditions derived

¹ See <http://www.iram.fr/IRAMFR/GILDAS> for more information about the GILDAS softwares (Pety 2005).

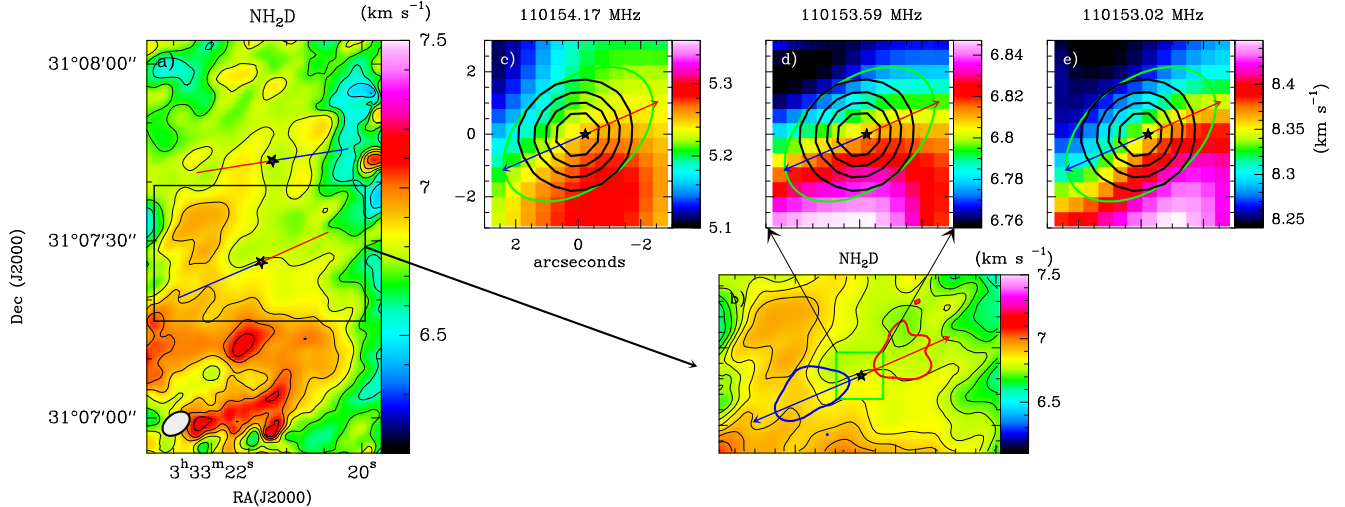


Fig. 2. Panel *a*: first-order moment map of the hyperfine component of the NH_2D line at 110 153.59 MHz. The stars indicate the positions of B1b-N and B1b-S. Blue and red arrows mark the outflow directions. Panel *b*: zoom around B1b-S of the image shown in *a*). Panels *c*, *d*, and *e*: are the first-order moment maps of the hyperfine components at the of 110 154.17, 110 153.59, and 110 153.03 MHz in a region of $3'' \times 3''$ around B1b-S. The same velocity pattern is observed in the three components, which corroborates that the velocity gradient observed in the main component is not an artifact due to self-absorption, but the signature of the pseudo-disk rotation. The green ellipse around the star indicates the beam size, and dark black contours correspond to the continuum emission at 145 GHz reported by Gerin et al. (2015). Continuum contour levels are 20% to 90% in steps of 20% of the peak emission.

by Gerin et al. (2015) in the outflow positions, $T_k = 20$ K and $n(\text{H}_2) = 6 \times 10^5 \text{ cm}^{-3}$ in B1b-N and $T_k = 30$ K and $n(\text{H}_2) = 5 \times 10^5 \text{ cm}^{-3}$ in B1b-S, we derive $N(\text{SO})/\Delta v < 1 \times 10^{13} \text{ cm}^{-2} \text{ km s}^{-1}$ and $N(^{13}\text{CO})/\Delta v < 2.4 \times 10^{14} \text{ cm}^{-2} \text{ km s}^{-1}$ in the B1b-N outflow; and $N(\text{SO})/\Delta v < 1.0 \times 10^{13} \text{ cm}^{-2} \text{ km s}^{-1}$ and $N(^{13}\text{CO})/\Delta v < 3.0 \times 10^{14} \text{ cm}^{-2} \text{ km s}^{-1}$ in the outflow associated with B1b-S. Gerin et al. (2015) determined CH_3OH column densities between $N(\text{CH}_3\text{OH})/\Delta v \sim 8 \times 10^{12} \text{ cm}^{-2} \text{ km s}^{-1}$ in B1b-N to $N(\text{CH}_3\text{OH})/\Delta v \sim 1 \times 10^{14} \text{ cm}^{-2} \text{ km s}^{-1}$ in the B1b-S blue lobe. Even assuming that the high-velocity gas is unresolved by the Gerin et al. (2015) observations and correcting for the lower angular resolution of our SO image (a factor of 3 in beam areas), the $N(\text{CH}_3\text{OH})/\Delta v$ would be a few $\times 10^{13} \text{ cm}^{-2} \text{ km s}^{-1}$ in the B1b-S blue lobe, which is larger than our limit to the SO column density per velocity interval. The SO abundance in the B1b-S outflow is therefore lower than a few 10^{-8} and hence might be similar to the abundance in the molecular cloud.

5. Infall signature and pseudo-disk

The line profiles of the ^{13}CO $1 \rightarrow 0$, C^{18}O $1 \rightarrow 0$ and the main component of the NH_2D line present self-absorption features at redshifted velocities. This is consistent with the infall signature expected toward young Class 0 objects. The redshifted absorption is not only detected at the protostar positions, but also at some positions in the outflow lobes (see Figs. 1 and A.1). This suggests that it is a signature of the global infall of the molecular filament, whose contraction has driven the formation of the two protostars. One alternative explanation could be that the apparent velocity gradient is due to the superposition of two filaments with slightly different velocities, but this interpretation would not explain the high star formation activity in the cloud.

Magnetohydrodynamic (MHD) simulations predict that the hydrostatic core is surrounded by a flat and slow rotating structure perpendicular to the outflow axis at these earliest stages of the star formation process. This structure is commonly referred to as a pseudo-disk (Hincelin et al. 2016). The detection of the pseudo-disk remains elusive because the high densities ($n(\text{H}_2) > 10^7 \text{ cm}^{-3}$) and still moderate temperatures of this com-

ponent (average kinetic temperature of 10–14 K) produce high molecular depletion factors for most species. Of the species studied in this Letter, only the NH_2D emission presents a maximum toward the protostar positions, and therefore it is our best candidate for the study of the pseudo-disk kinematics.

In Fig. 2b we show the first-order moment map of the main hyperfine component of the NH_2D $1_{1,1a} \rightarrow 1_{0,1s}$ line in the surroundings of B1b-S. The overall east-west velocity gradient that is clearly observed along the whole filament is distorted in the vicinity of B1b-S, where the velocity gradient becomes perpendicular to the axis of the outflow driven by this protostar. This behavior is also observed in the satellite components at 110 154.17 and 110 153.03 MHz. The detection of the same velocity pattern in the three hyperfine components confirms that the velocity gradient is real and not an artifact of the self-absorption feature. We interpret this gradient as the signature of the pseudo-disk rotation predicted by MHD simulations. According to the rotation axis, the major axis of the pseudo-disk must be located at a PA of 45° as measured from north to east. This is also consistent with the elongation of the disk detected with ALMA toward this source Gerin et al. (2017). We did not detect any such rotation signature toward B1b-N, which is more deeply embedded. The angular resolution of our observations is not sufficient to fully resolve the pseudo-disk around B1b-S, and the detected velocity gradient, $0.2 \text{ m s}^{-1} \text{ au}^{-1}$, is a lower limit to the rotation velocity. Toward B1b-S, the NH_2D $1_{1,1a} \rightarrow 1_{0,1s}$ line presents weak wings that are not detected toward adjacent positions. If these wings were caused by rotation, the rotation velocity would be $\sim 2.5 \text{ km s}^{-1}$, which is comparable to the rotation velocities predicted by the MHD simulations (Galli & Shu 1993; Hincelin et al. 2016).

We imaged only one transition per species, and therefore our abundance estimates involve large uncertainties. In addition, all the lines may be optically thick in the high-extinction regions around the protostars. Fortunately, the hyperfine structure of NH_2D allows us to estimate the line opacity and overcome these limitations. We fit the NH_2D hyperfine lines assuming the same excitation temperature for all the hyperfine components. This procedure allows us to derive the main line opacities. We obtain opacities in the range of ~ 0.24 – 2.0 (see Table A.2).

Assuming that the emission uniformly fills the beam, we derive $N(\text{NH}_2\text{D}) \sim 6.0 \times 10^{14} \text{ cm}^{-2}$ and $3.5 \times 10^{14} \text{ cm}^{-2}$ toward B1b-N and S, respectively (Table A.3). Using the 1.2 mm map reported by Daniel et al. (2013), a constant dust temperature of 12 K and $\kappa = 0.01 \text{ cm}^2 \text{ g}^{-1}$, we estimate $N(\text{H}_2) = 1.0 \times 10^{23} \text{ cm}^{-2}$ and $1.3 \times 10^{23} \text{ cm}^{-2}$ toward B1b-N and S, respectively. Based on these estimates, we derive NH_2D abundances of $\sim 6 \times 10^{-9}$ and $\sim 2 \times 10^{-9}$ for B1b-N and S. These values are in agreement with those derived by Daniel et al. (2013) for the inner $R < 4000$ au part of the envelope. For SO, we assume that the lines are thermalized at $T_k = 10$ K and derive $N(\text{SO}) \sim 1.8 \times 10^{14} \text{ cm}^{-2}$ in B1b-N and $N(\text{SO}) \sim 1.5 \times 10^{14} \text{ cm}^{-2}$ in B1b-S. The SO abundances are $\approx 2 \times 10^{-9}$ in B1b-N and 1×10^{-9} in B1b-S, a factor of ~ 10 lower than the single-dish estimate by Fuente et al. (2016).

6. Modeling the gas chemistry

Gerin et al. (2017) compared recent ALMA continuum observations at 349 GHz with the model of a strongly magnetized, turbulent, collapsing $1 M_\odot$ core from Hennebelle et al. (2016), with ambipolar diffusion as in Masson et al. (2016), at an inclination angle of 20° . The initial core density and temperature were uniform, $\rho_0 = 9.4 \times 10^{-18} \text{ g cm}^{-3}$ and $T = 10$ K, and the mass-to-flux ratio $\mu = 2$. After 6.4×10^4 yr, the simulations show a structure consistent with ALMA and NOEMA observations, with a disk of $R = 50\text{--}75$ au ($\rho \sim 10^{-14}\text{--}10^{-11} \text{ g cm}^{-3}$), a pseudo-disk of $R = 700$ au ($\rho \sim 10^{-17}\text{--}10^{-14} \text{ g cm}^{-3}$), and an outflow that extends up to 1100 au. In this model the gas thermal behavior is described by the barotropic law $T_K = 10 \times (1 + (\rho/\rho_c)^{4/3})^{0.5}$. We used the pseudo-time-dependent model described by Pacheco-Vázquez et al. (2015, 2016) to calculate the abundances of CO, H₂CO, SO, and NH₃ at $t = 10^5$ yr assuming the physical conditions given by the barotropic law. The chemical model is an updated version of the model reported by Agúndez et al. (2008) and Fuente et al. (2010), and it includes a complete gas-phase chemical network for C, O, N, and S, adsorption onto dust grains and desorption processes such as thermal evaporation, photodesorption, and desorption induced by cosmic rays. The abundances of most molecules have not reached the steady-state value at these early times, and the results are sensitive to the initial conditions and chemical age. We repeated the calculations for two sets of initial conditions that are representative of i) the dark cloud case (low-metallicity case of Wiebe et al. 2003) and ii) solar abundances. In both cases, we adopted $\zeta = 5 \times 10^{-17} \text{ s}^{-1}$ as derived by Fuente et al. (2016). As a general behavior, the abundances of the four molecules are heavily depleted in the pseudo-disk and increase again in the disk where the temperature rises above 100 K (see Fig. 3). The abundance of H₂CO follows that of CO, which starts to freeze out onto the grains in the envelope. The SO and NH₃ abundances remain relatively high for H₂ densities below 10^7 cm^{-3} ($\rho = 3.8 \times 10^{-17} \text{ g cm}^{-3}$). The abundance of SO reaches its maximum value at around $R = 700\text{--}1000$ au, that is, in the outer part of the pseudo-disk. This model explains the morphology in B1b quite well, where the SO emission surrounds the NH₂D cores while ¹³CO and C¹⁸O are tracing the external envelope, although it fails to account for the observed abundances. We note that surface chemistry is not included, and the abundance of some molecules such as NH₃ could therefore be underestimated. Unfortunately, our model does not include deuterium chemistry for further comparison.

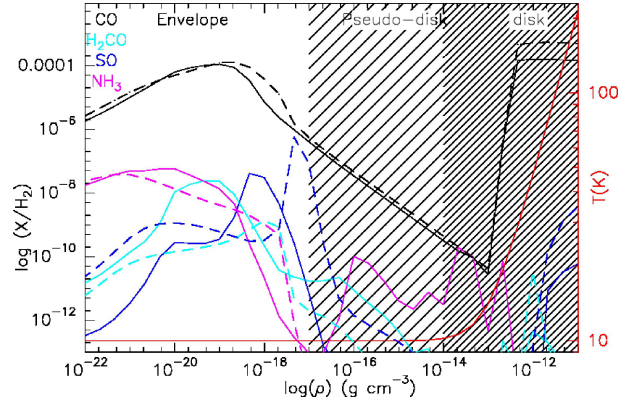


Fig. 3. Chemical model predictions for $t = 10^5$ yr assuming as initial abundances the low-metallicity case of Wiebe et al. (2003) (continuous lines) and solar abundances (dashed lines). We indicate the parameter space corresponding to the envelope, pseudo-disk, and disk according with the MHD simulations reported by Gerin et al. (2017).

7. Conclusions

The combination of NOEMA and 30 m data reveals for the first time the physical structure of the young protostellar system formed by B1b-N and B1b-S. The two protostellar objects are embedded in an elongated condensation with a velocity gradient in the east-west direction that is reminiscent of an axial collapse. Our NH₂D data allow us to detect the pseudo-disk associated with each protostar. Moreover, we find evidence of rotation in the pseudo-disk associated with B1b-S. The envelope, outflows, and pseudo-disks can be chemically segregated: the envelope is detected in the CO isotopologues; the outflows, in H₂CO and CH₃OH; and the pseudo-disks, in NH₂D. The SO emission seems to come from the outer part of the pseudo-disk. It is interesting to note that SO is not detected in the outflows, although the sensitivity of our observations does not allow us to significantly constrain its abundance in the high-velocity gas.

Acknowledgements. We thank the Spanish MINECO for funding support from grants CSD2009-00038, AYA2012-32032, AYA2016-75066-C2-1/2-P, and ERC under ERC-2013-SyG, G. A. 610256 NANOCOSMOS. E.R. and M.G. thank the INSU/CNRS program PCMI for funding.

References

- Agúndez, M., Cernicharo, J., & Goicoechea, J. R. 2008, [A&A](#), **483**, 831
- Daniel, F., Gérin, M., Roueff, E., et al. 2013, [A&A](#), **560**, A3
- Fuente, A., Cernicharo, J., Agúndez, M., et al. 2010, [A&A](#), **524**, A19
- Fuente, A., Cernicharo, J., Roueff, E., et al. 2016, [A&A](#), **593**, A94
- Galli, D., & Shu, F. H. 1993, [ApJ](#), **417**, 220
- Gerin, M., Pety, J., Fuente, A., et al. 2015, [A&A](#), **577**, L2
- Gerin, M., Pety, J., Commerçon, B., et al. 2017, [A&A](#), **606**, A35
- Hennebelle, P., Commerçon, B., Chabrier, G., & Marchand, P. 2016, [ApJ](#), **830**, L8
- Hincelin, U., Commerçon, B., Wakelam, V., et al. 2016, [ApJ](#), **822**, 12
- Huang, Y.-H., & Hirano, N. 2013, [ApJ](#), **766**, 131
- Lis, D. C., Wootten, A., Gerin, M., & Roueff, E. 2010, [ApJ](#), **710**, L49
- Masson, J., Chabrier, G., Hennebelle, P., Vaytet, N., & Commerçon, B. 2016, [A&A](#), **587**, A32
- Pacheco-Vázquez, S., Fuente, A., Agúndez, M., et al. 2015, [A&A](#), **578**, A81
- Pacheco-Vázquez, S., Fuente, A., Baruteau, C., et al. 2016, [A&A](#), **589**, A60
- Pety, J. 2005, in SF2A-2005: Semaine de l’Astrophysique Francaise, eds. F. Casoli, T. Contini, J. M. Hameury, & L. Pagani, 721
- Pezzuto, S., Elia, D., Schisano, E., et al. 2012, [A&A](#), **547**, A54
- Wiebe, D., Semenov, D., & Henning, T. 2003, [A&A](#), **399**, 197

Appendix A: Additional tables and figures

Table A.1. Summary of observations.

Line	Freq (MHz)	E_{upp} (K)	NOEMA			NOEMA+30 m		
			Beam ('')	PA($^{\circ}$)	rms(K) ¹	Beam ('')	PA($^{\circ}$)	rms(K) ¹
$\text{C}^{18}\text{O} \ 1 \rightarrow 0$	109 782.17	5.3	5.01×3.41	-52	0.13	5.48×3.45	-54	0.12
$^{13}\text{CO} \ 1 \rightarrow 0$	110 201.35	5.3	4.72×3.21	-51	0.13	5.38×3.38	-53	0.12
$\text{NH}_2\text{D} \ 1_{1,1}a \rightarrow 1_{0,1}s$	110 153.59	21.3	4.74×3.23	-51	0.16	5.21×3.38	-54	0.14
$\text{SO} \ 3_2 \rightarrow 2_1$	109 252.22	21.1	4.75×3.25	-52	0.15	5.44×3.44	-52	0.12

Notes. ⁽¹⁾ rms in a velocity channel of 0.2 km s^{-1} for C^{18}O , ^{13}CO , and SO, and of 0.14 km s^{-1} for NH_2D .

Table A.2. Line fits.

Offsets ¹		C^{18}O			SO			NH ₂ D			
		Area (K km s ⁻¹)	V_{lsr} (km s ⁻¹)	ΔV (km s ⁻¹)	Area (K km s ⁻¹)	V_{lsr} (km s ⁻¹)	ΔV (km s ⁻¹)	$(T_{\text{ex}} - T_{\text{bg}}) \times \tau$ (K)	V_{lsr} (km s ⁻¹)	ΔV (km s ⁻¹)	τ
B1b-N	(0, 0)	7.50(0.09)	6.9(0.1)	1.4(0.1)	2.02(0.05)	6.6(0.1)	0.7(0.1)	4.51(0.31)	6.7(0.1)	0.9(0.1)	1.7(0.2)
N-out#1	(-5, 1)	6.72(0.08)	6.8(0.1)	1.2(0.1)	2.49(0.06)	6.6(0.1)	0.6(0.1)	1.60(0.17)	6.9(0.1)	1.3(0.1)	0.4(0.3)
B1b-S	(0, 0)	7.22(0.09)	6.8(0.1)	1.6(0.1)	1.89(0.07)	6.9(0.1)	0.9(0.1)	6.18(0.28)	6.8(0.1)	0.7(0.1)	1.5(0.2)
S-out#1	(6, -2)	6.54(0.10)	6.9(0.1)	1.6(0.1)	1.94(0.06)	6.9(0.1)	0.8(0.1)	4.20 (0.32)	6.8(0.1)	0.6(0.1)	1.5(0.3)
S-out#2	(-9, 6)	4.83(0.08)	6.9(0.1)	1.2(0.1)	2.21(0.06)	6.6(0.1)	0.7(0.1)				
S-out#3	(-8, 10)	4.79(0.07)	6.9(0.1)	1.3(0.1)	2.17(0.06)	6.6(0.1)	0.7(0.1)				
S-out#4	(-7, 1)	5.52(0.08)	6.9(0.1)	1.4(0.1)	2.66(0.07)	6.7(0.1)	0.9(0.1)				

Notes. ⁽¹⁾ Offsets are given in arcseconds relative to each protostellar object.

Table A.3. Molecular column densities.

Offsets	$N(\text{SO})^a$	$N(\text{NH}_2\text{D})^b$	$N(\text{NH}_2\text{D})/N(\text{SO})$
B1b-N (0,0)	1.8×10^{14}	6.0×10^{14}	~3.3
B1b-S (0,0)	1.5×10^{14}	3.5×10^{14}	~2.3

Notes. ^(a) Assuming local thermodynamic equilibrium with $T_k = 10 \text{ K}$. ^(b) Using the opacities and excitation temperatures derived from the line fitting (see Table A.2).

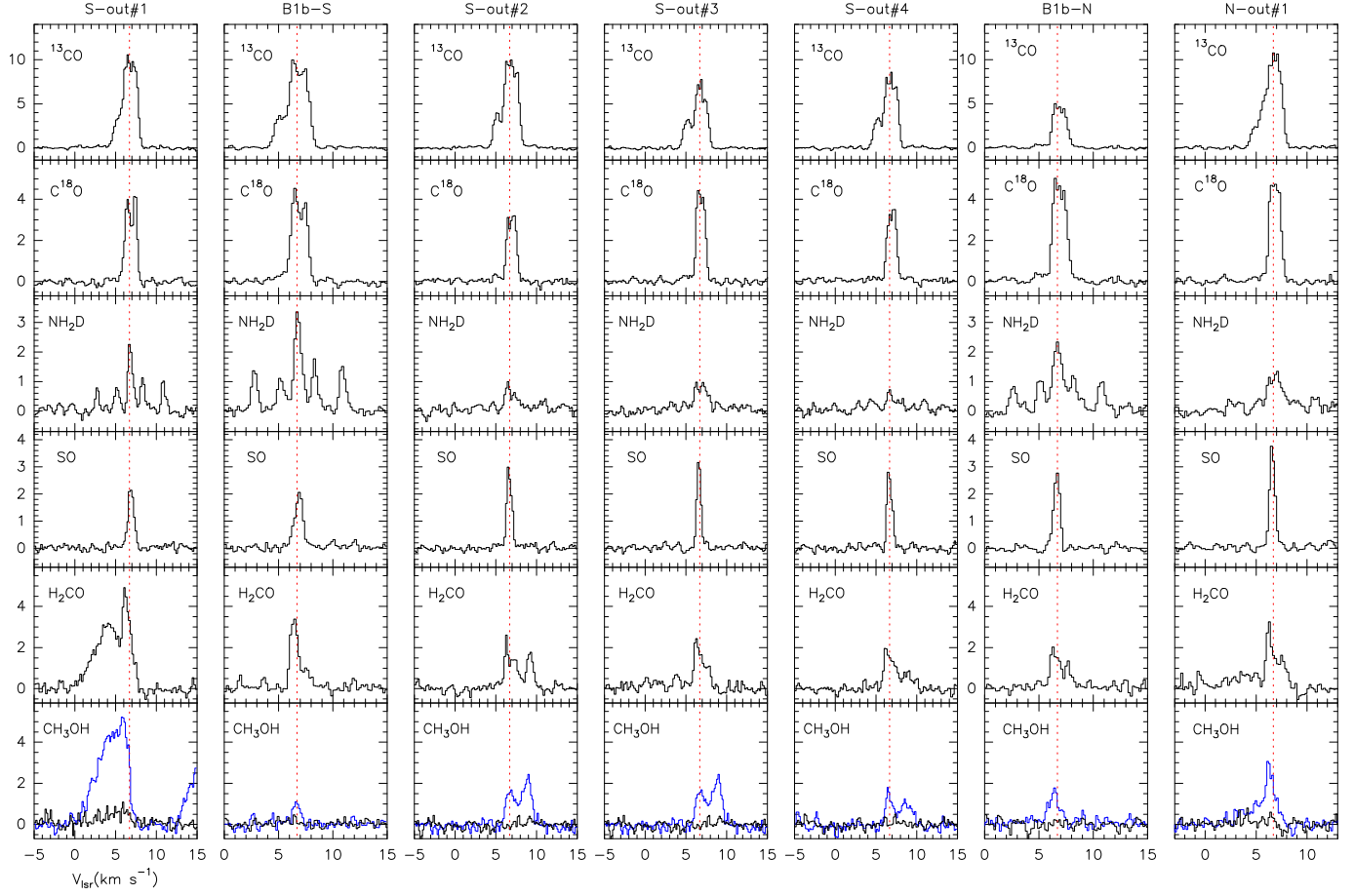


Fig. A.1. Interferometric spectra toward a set of selected positions (intensities in K). In addition to our data, we show the spectra of the H_2CO $2_{0,2}-1_{0,1}$, CH_3OH 3_0-2_0 A (blue) and CH_3OH 3_2-2_2 E (black) lines published by [Gerin et al. \(2015\)](#). The systemic velocity, $v_{\text{lsr}} = 6.7 \text{ km s}^{-1}$, is marked with a dashed red line.

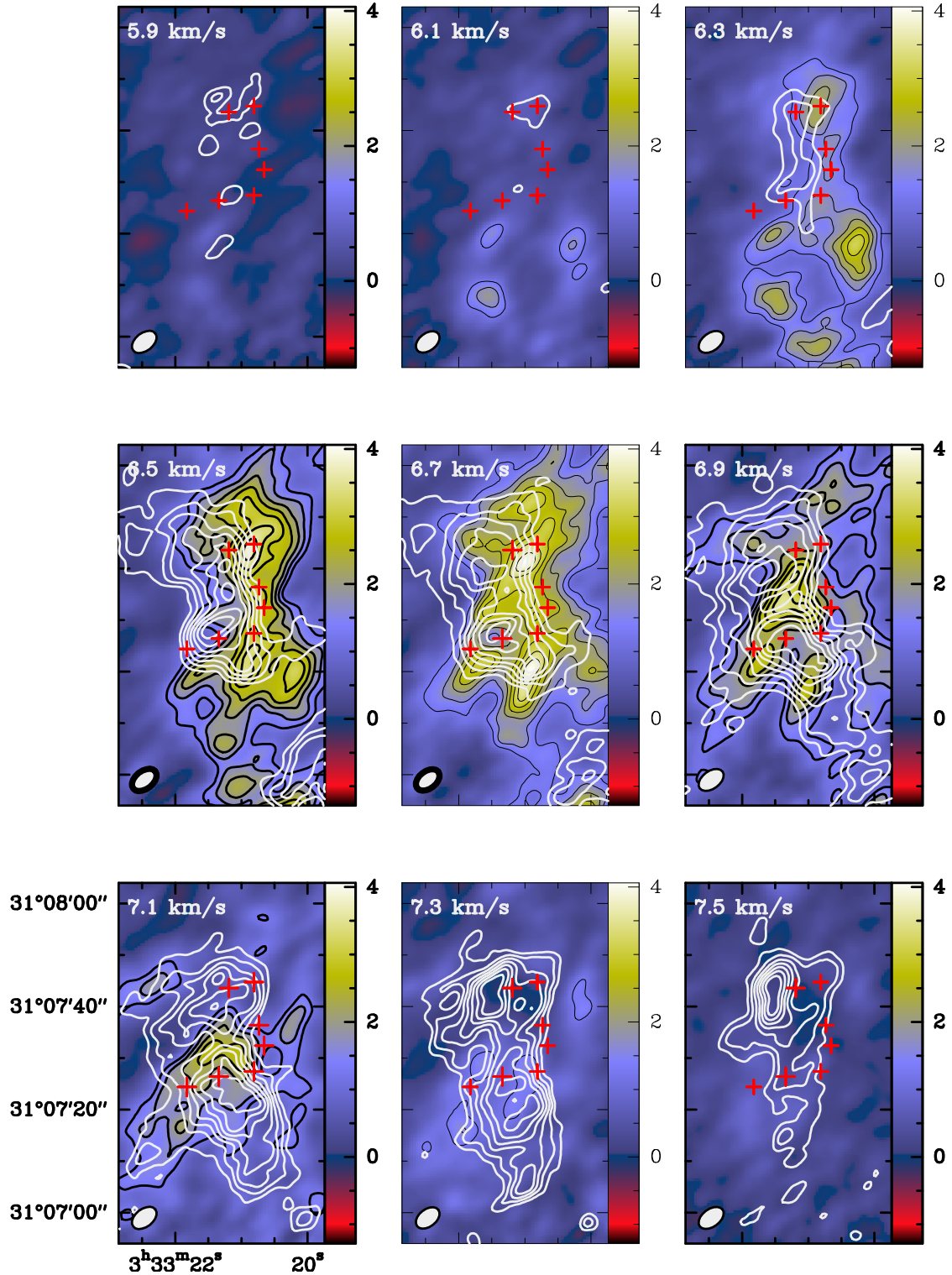


Fig. A.2. Channel maps of the emission of the $\text{SO } 3_2 \rightarrow 2_1$ (color map) and the main component of the $\text{NH}_2\text{D } 1_{1,1}a \rightarrow 1_{0,1}s$ (white contours) lines. The images have been created by merging the NOEMA data with the short spacing obtained with the IRAM 30 m telescope. The channel velocity is marked at the top of the panel. Red crosses indicate the positions studied in detail in this Letter.